Friction **11**(3): 460–472 (2023)
https://doi.org/10.1007/s40544-022-0621-x
ISSN 2223-7690
CN 10-1237/TH
RESEARCH ARTICLE

High-temperature wear mechanisms of TiNbWN films: Role of nanocrystalline oxides formation

Leilei CHEN[1,2], Zhenyu ZHANG[1,*], Ming LOU[2], Kai XU[2], Lu WANG[2], Fanning MENG[1], Denis MUSIC[3], Keke CHANG[2,*]

[1] *Key Laboratory for Precision and Non-Traditional Machining Technology of Ministry of Education, Dalian University of Technology, Dalian 116024, China*

[2] *Key Laboratory of Marine Materials and Related Technologies, Zhejiang Key Laboratory of Marine Materials and Protective Technologies, Ningbo Institute of Materials Technology and Engineering, Chinese Academy of Sciences, Ningbo 315201, China*

[3] *Department of Materials Science and Applied Mathematics, Malmö University, Malmö 20506, Sweden*

Received: 12 January 2021 / Revised: 22 February 2022 / Accepted: 08 March 2022

© The author(s) 2022.

Abstract: Refractory high/medium entropy nitrides (HENs/MENs) exhibit comprehensive application prospects as protective films on mechanical parts, particularly those subjected to sliding contacts at elevated temperatures. In this study, a new MEN system TiNbWN, forming a single fcc solution, is designed and its wear performance at temperatures ranging from 25 to 750 °C is explored. The wear mechanisms can be rationalized by examining the subsurface microstructural evolutions using the transmission electron microscopy as well as calculating the phase diagrams and interfacial adhesion behavior employing calculation of phase diagram (CALPHAD) and density functional theory (DFT). To be specific, increased wear losses occur in a temperature range of 25–600 °C, being predominantly caused by the thermally-induced hardness degradation; whereas at the ultimate temperature (750 °C), the wear loss is refrained due to the formation of nanocrystalline oxides (W_nO_{3n-2}, TiO_2, and γTiO_x), as synergistically revealed by microscopy and CALPHAD, which not only enhance the mechanical properties of the pristine nitride film, but also act as solid lubricants, reducing the interfacial adhesion. Thus, our work delineates the role of the *in situ* formed nanocrystalline oxides in the wear mechanism transition of TiNbWN thin films, which could shed light on the high-temperature wear behavior of refractory HEN/MEN films.

Keywords: high/medium entropy nitrides (HENs/MENs); TiNbWN thin films; wear mechanisms; nanocrystalline oxides

1 Introduction

High/medium entropy alloys (HEAs/MEAs) containing elements in near-equiatomic proportions normally with a single-phase structure have attracted extensive attention as they demonstrate potential combinatorial properties that are not attainable in conventional alloys [1–3]. Recently, incorporation of p-block elements such as nitrogen (N), carbon (C), and boron (B) has led to the development of new high/medium entropy materials, which are high/medium entropy nitrides (HENs/MENs), high/medium entropy carbides (HECs/MECs), and high/medium entropy borides (HEBs/MEBs) [4–7]. The HENs/MENs possess superiorities in terms of high-temperature thermal stability, oxidation resistance, and mechanical properties due to the sluggish diffusion and solid solution strengthening effects, being qualified as protective films on the mechanical parts that operate at varying temperatures [5, 7–9].

* Corresponding authors: Zhenyu ZHANG, E-mail: zzy@dlut.edu.cn; Keke CHANG, E-mail: changkeke@nimte.ac.cn

Herein, toward high-temperature applications, we add the refractory metal elements, niobium (Nb) and tungsten (W), into the benchmark binary nitride system, titanium nitride (TiN), to design a novel MEN system, TiNbWN. Even though there is a paucity of studies on the TiNbWN films, the structure–property relationships for the ternary TiNbN and TiWN films have been tackled. For example, Baran [10] reported that the TiNbN film contained a single TiN-type fcc phase, with a microhardness (*H*) value as high as 24 GPa. Serro et al. [11] further compared the wear resistance of TiN, TiNbN, and TiCN thin films for biomedical applications, whereby the TiNbN film performed best in the presence of albumin. For the TiWN films, on the other hand, the phase transformation from βW to an fcc solution was observed with an increasing N concentration [12–14]. Besides, the mechanical properties of the TiWN film also depend on the N and W concentrations. For instance, the hardness values of TiWN films varied from 23 to 50 GPa in a composition range of 30–57 at% N [15]; while they changed from 13.9 to 26.3 GPa in a composition range of 0–50.6 at% W, following the variations in crystallinity [16–18].

The wear failure mechanisms in high-temperature protective films are one of the most fundamental issues to be addressed for a prolonged service lifetime [19–21]. In particular, the sliding-induced oxidation that can significantly influence the tribological performance of materials has been considered to be an interesting topic [19, 22–24]. After their discovery in the 1930s [25], specific types of oxides, formed on metal and alloy surfaces during the course of sliding, have been recognized as important constituents for generating protective tribolayers at elevated temperatures, which could decrease metal–metal contacts and alleviate wear losses [26–29]. For non-oxide ceramics and ceramic coatings in general, however, the generated oxides may play a different role in friction and wear performances [30–33]. For instance, the wear resistance of the transitional metal nitrides strongly depends on their mechanical properties, especially surface hardness [32], whereas the sliding-induced oxidation of transitional metal nitrides would generally decrease the surface hardness due to the formation of an oxide layer, leading to the so-called "oxidational wear" [30]. The generated oxides at elevated temperatures, on the other hand, could act as solid lubricants in certain scenarios and reduce the friction [32, 33]. Specifically, some functional oxides, such as the Magnéli phase [31], can effectively improve the tribological performances of ceramic materials. The Magnéli phases, defined as a homologous series of compounds with closely related lamellar structures [34–36], can serve as effective solid lubricants to improve friction and wear performance when generated in a large quantity [31, 37–39].

In this work, we design and synthesize a new multicomponent TiNbWN thin film with an fcc structure based on the high/medium entropy concept, and subsequently examine its wear resistance by performing the tribological tests at 25, 300, 600, and 750 °C. With an aid of electron microscopy and spectroscopic methods, the wear mechanism transition and nano-oxide formation are identified as a function of temperature. The subsurface microstructures of the worn samples, the phase diagrams of the W–O system, as well as the calculated adsorption energies of relevant interaction counterparts, are further utilized to address the following specific questions: (1) How can the wear behavior of TiNbWN thin films at varying temperatures be described; (2) what is the role of the *in situ* formed nano-oxides in the wear mechanism transition.

2 Experimental details

2.1 Film deposition

The multicomponent TiNbWN thin film was reactively magnetron sputtered in mixed N_2/Ar (20/100 sccm gas flow rate) discharges on 304 stainless steel (304ss) substrates using a custom-built system. Prior to the deposition, the synthesis chamber was first pumped down at 25 °C to a base pressure lower than 5×10^{-4} Pa; then, the substrate holder was gradually heated up to 800 °C. A TiNbW alloy target (Ti = 33.3 at%, Nb = 34.9 at%, W = 31.8 at%; purity 99.99%) was used to synthesize the thin film, which was driven by direct current (DC) power supply at a power density of 1.06 W/cm^2. The total working pressure (Ar + N_2) in the chamber was 1.0 Pa. A pulsed-DC bias voltage of −100 V (at a pulse frequency of 20 kHz and a pulse duty ratio of 50%) was applied on the substrate holder, which rotated at the speed of 20 rpm during the

deposition. The distance between the target and the substrate was 11 cm.

2.2 Tribological testing

The tribological tests of the TiNbWN thin film were conducted against 316 stainless steel (316ss) balls with 6 mm in diameter at temperatures ranging from 25 to 750 °C under ambient atmosphere (~35% relative humidity) using Anton–Paar tribometer (THT1000, Anton-Paar) equipped with a rotational module. An applied normal load of 1 N and a linear sliding speed of 3 mm/s were employed in all the tests, yielding a maximum Hertzian contact pressure of ~800 MPa. The radius of the wear track was 3 mm, and the test time was 20 min that corresponded to a total sliding distance of 18 m. After the completion of each sliding test, the volumetric wear losses were acquired from the surface profile traces across the wear track using surface profilometry.

2.3 Film characterization

The surface and cross-sectional morphologies of the deposited TiNbWN thin film were studied using a field-emission scanning electron microscope (FE-SEM; Quanta FEG 250, FEI), while the elemental compositions of the film were measured by the energy dispersive X-ray spectrometry (EDS). The accelerating voltage of 15 kV was applied. The crystal structure of the film was investigated using the X-ray diffraction analysis (XRD; D8 Advance, Bruker) with Cu Kα radiation (λ = 1.5406 Å). The power settings were 40 mA for the current and 40 kV for the voltage. The H and elastic modulus (E) of the film were determined using a nano-indenter (G200, MTS) with a Berkovich diamond tip within the continuous stiffness measurement mode, following the method by Oliver and Pharr [40]. The reported values of H and E were the average of five measurements. The Poisson ratio (v) of 0.18 was assumed.

After sliding tests, the types of oxides induced by sliding contact were studied using a micro-Raman spectrometer (InVia Reflex, Renishaw) that operated with a laser wavelength of 532 nm. Cross-sections of the worn samples were prepared using a focused ion beam (FIB; Auriga, Zeiss) "lift-out" technique, with the subsurface microstructure evolutions and elemental distributions examined using a transmission electron microscope (TEM; Talos F200, Thermo Fisher) and a high-resolution TEM (HRTEM) equipped with a windowless energy dispersive spectrometer. The accelerating voltage of 20 kV was applied during microscopy.

2.4 Computational methods

The adsorption energy was calculated using *ab initio* calculations based on density functional theory (DFT) [41], which was carried out in the Vienna *ab initio* simulation package (VASP) [42]. Projector augmented wave potentials and the generalized gradient approximation were used in all calculations [43, 44]. A total energy cut-off of 500 eV was applied for the adsorption calculations. The Brillouin zone was sampled using gamma-centered Monkhorst–Pack k-point grids. The TiNbWN(001), TiO_2(001), and WO_3(001) surfaces were modeled as slabs with a vacuum thickness of 10 Å. Supercells containing 24 atoms were constructed for TiNbWN(001) and TiO_2(001) surfaces, while a supercell containing 40 atoms was chosen for the WO_3(001) surface to enable a suitable slab thickness. The top four-atom layers near the vacuum layer were relaxed until the force on each of them was less than 0.01 eV/Å, while the other atoms were fixed to mimic a bulk behavior. Herein, we assumed that the sliding interfaces comprised of the pristine/oxidized film surface and oxidized the counterpart atoms (stainless steel) being represented by a vertically aligned Fe–O molecule with either the Fe or O atom approaching the coating surface. The adsorption energies (E_{ads}) were calculated by Eq. (1):

$$E_{ads} = E_{FeO/slab} - E_{slab} - E_{FeO} \quad (1)$$

where $E_{FeO/slab}$ and E_{slab} are the total energy of the (001) surface of the slab models with FeO and without it, respectively; and E_{FeO} is the total energy of the FeO molecule, calculated in a cell with a dimension of 10 Å × 10 Å × 10 Å.

3 Results and discussion

3.1 Microstructures and properties

The surface and cross-sectional morphologies of the

TiNbWN thin film are shown in Fig. 1. A facetted microstructure is present based on the top-view of the thin film, while its cross-sectional SEM image shows a distinct columnar growth, a common feature for sputtered thin films. The elemental compositions of the thin film measured by EDS confirmed that the Ti, Nb, and W have similar atomic concentrations (Ti = 21 at%, Nb = 19 at%, and W = 23 at%), and the N content is 37 at%. The XRD pattern was obtained over 20°–90° to investigate the constitution of the TiNbWN thin film, as shown in Fig. 1(c). The TiNbWN thin film can be described as a TiN-type single fcc phase (PDF#28-1420), in which the Nb and W atoms occupy the Ti sites. The fact that the TiNbWN film contains a single solution phase can be supported by the structural similarities of the binary nitrides of TiN, NbN, and γWN, which exhibit the same fcc phase with rather similar lattice parameters (a (TiN) = ~0.42 nm, a (NbN) = ~0.44 nm, and a (γWN) = ~0.41 nm) [45–47]. The characteristic peaks in the XRD pattern slightly deviated to smaller values compared with that of the TiN phase, indicating that the interplanar spacing of the fcc solution in the TiNbWN thin film was increased by dissolving Nb and W. The strongest peak corresponded to the (111) crystallographic plane, implying the preferred growth of the film deposited.

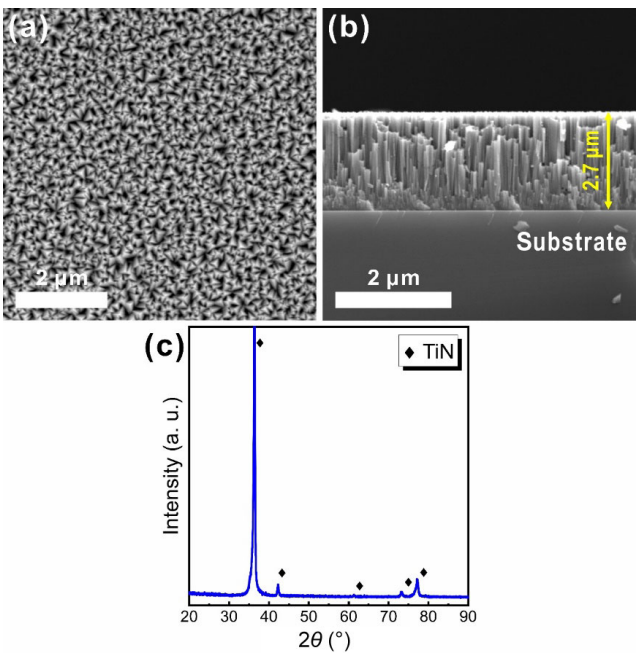

Fig. 1 Morphologies and microstructural features of the as-deposited TiNbWN thin film: (a) surface and (b) cross-sectional SEM images; (c) XRD pattern.

3.2 Sliding wear performance

Figure 2(a) shows the wear losses of the TiNbWN film sliding against 316ss as a function of the sliding temperature, as well as the variation in H with the increasing oxidation temperature. In the temperature range of 25–600 °C, the hardness of the thin film sharply decreased while the wear losses increased dramatically with increasing temperature. Interestingly, at a temperature of 750 °C, the hardness of the thin film slightly increased, and the wear losses simultaneously decreased. The H/E and $H^3/(E^*)^2$ ratios (where $E^* = E/(1-v^2)$ is the effective Young's modulus [48]) were then calculated based on the obtained H and E, as shown in Fig. 2(b). The H/E value implies the resistance against elastic strain to failure [49], while the $H^3/(E^*)^2$ value indicates the resistance to plastic deformation [48]. Accordingly, with the increase of temperature, the TiNbWN film experiences first a decrease then a slight increase in the deformation resistance. It remains to be explored, but it seems that there is a change in microstructure at a temperature around 750 °C, which in turn may be a cause for the improved mechanical and wear properties of the thin film.

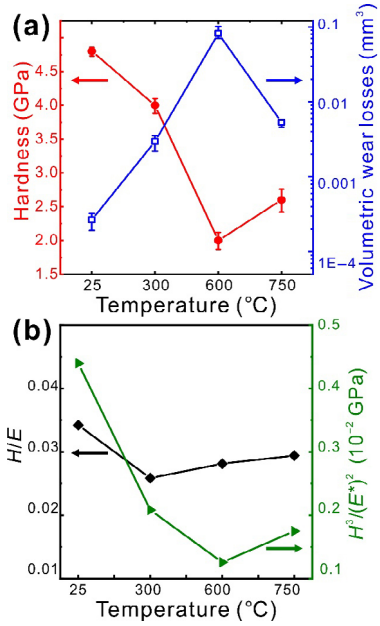

Fig. 2 (a) Volumetric wear losses for TiNbWN films sliding against 316ss stainless steel at an applied load of 1 N for a total sliding distance of 18 m and the change in hardness (H) of the films as a function of temperature. (b) H/E and $H^3/(E^*)^2$ ratios of the TiNbWN film plotted against temperature.

Representative SEM images of the worn surfaces of the TiNbWN thin film after sliding against 316ss and the corresponding two-dimensional (2D) line scans of the wear tracks are shown in Fig. 3. The wear tracks generated at 25 °C exhibit a smooth appearance with some transferred materials attached, while those formed at 300 °C contain distinct grooves parallel to the sliding direction. Severe wear damage of the thin film occurred when the sliding temperature increased to 600 °C, as the film was entirely worn out, exposing the bare steel substrate. The thin film after sliding test at 750 °C, however, maintains a relatively intact surface with some grooves generated and the squeeze-out of materials occurring at certain locations. The 2D line scans of the wear tracks are shown in Fig. 3(e), in which the wear track at 600 °C reveals the largest width and depth, followed by the wear track formed at 750 and 300 °C. By analyzing the results presented in Figs. 2 and 3, the wear behavior of the TiNbWN thin film at varying temperatures can be preliminarily depicted as follows: (i) The thin film exhibits a high surface hardness at 25 °C, thus possessing a relatively low wear loss according to the Archard equation [50]; (ii) when temperature increases, plastic deformation occurs during sliding due to the thermally-induced mechanical property attenuation, and as a result, the wear loss monotonously increases up to 600 °C; (iii) further increase of the temperature, however, reduces the wear loss, indicating a transition in the wear mechanisms. Section 3.3 will focus on the subsurface microstructural features at both 25 and 750 °C to unravel this wear mechanism transition.

3.3 Subsurface microstructures at different temperatures

Figure 4 shows the subsurface microstructure of the TiNbWN thin film after sliding at 25 °C. An obvious deformation zone was observed right beneath the top sliding surface of the thin film, where the columnar structure was slightly bent towards the sliding direction under the effect of shear stresses. The equivalent plastic strains were estimated to be 0.202 at a depth of 600 nm from the top surface [51]. Associated with the accumulation of shear strains, plenty of microcracks that penetrated across the columnar structure were observed, which can be understood as the harbinger of catastrophic fracture. In addition, an amorphous oxide layer with a thickness of ~130 nm formed on the contact surfaces, while the elemental distribution mappings in Fig. 4(b) confirmed the high concentrations of O and Ti in the oxide layer, and the selected area electron diffraction (SAED) pattern in Fig. 4(c) further revealed its amorphous nature. The composition of this amorphous layer obtained using the EDS was

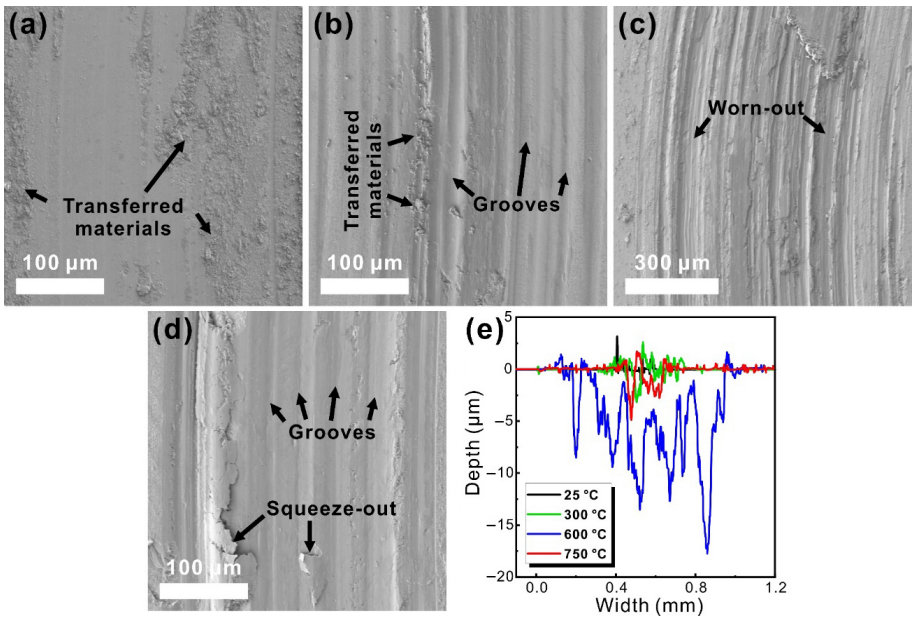

Fig. 3 Representative SEM images of the worn surfaces of the TiNbWN thin film after sliding against 316ss stainless steel at (a) 25 °C, (b) 300 °C, (c) 600 °C, and (d) 750 °C. (e) Comparison of typical 2D line scans of the wear tracks formed at different temperatures.

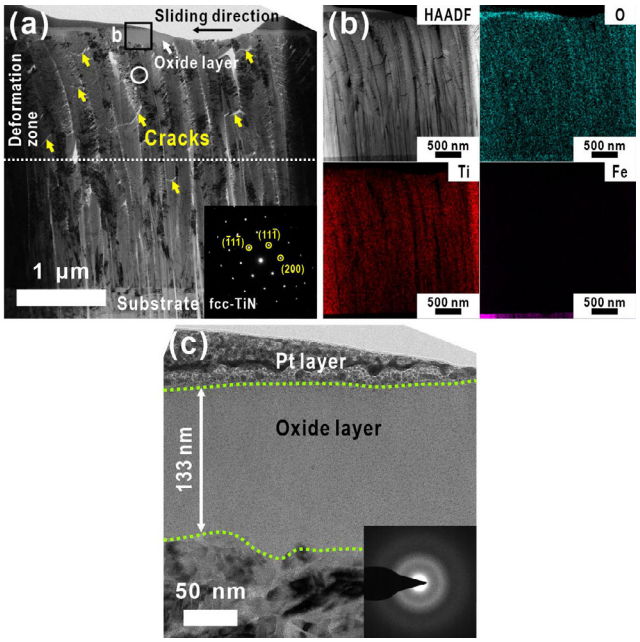

Fig. 4 (a) Cross-sectional bright-field TEM image of the TiNbWN thin film after sliding against 316ss stainless steel for a test distance of 18 m at 25 °C with an SAED pattern acquired from the region marked with a white circle and (b) corresponding high angle annular dark field (HAADF) images and elemental distribution mappings. (c) HRTEM image of the region marked as "b" in (a) with the SAED pattern of the oxide layer shown in the inset.

$Ti_{6.8}Nb_{7.3}W_{7.6}N_{6.3}O_{72.0}$ (at%). Thus, the sliding wear of TiNbWN thin films at 25 °C can be characterized by the simultaneous operation of mechanical and oxidational wear mechanisms, and the formation of an amorphous oxide layer is conceivably beneficial to restrain the wear loss, but only to a limited extent.

The subsurface microstructures of the TiNbWN thin film after sliding tests against 316ss for a total sliding distance of 18 m at 750 °C are shown in Fig. 5. As observed, the film at this condition exhibits a homologous morphology with the disappearing of the columnar structure shown in Fig. 4. The film is composed of dark and white nano-size particles in both the near-surface region (Fig. 5(b)) and the region far from the top surface (Fig. 5(c)). The SAED pattern (Fig. 5(d)) identifies the oxides as a mixture of W_nO_{3n-2} (PDF#05-0386) and TiO_2 (PDF#87-0710) in addition to γTiO_x (PDF#08-0117). The γTiO_x oxide is a high-temperature phase with a wide solubility range of composition, which crystallizes in the halite (NaCl-type fcc) structure [52]. EDS mappings of the film confirm (Fig. 5(e)) the occurrence of segregation upon high-temperature oxidation, with the presence of W-rich and Ti-rich nanoparticles. The chemical

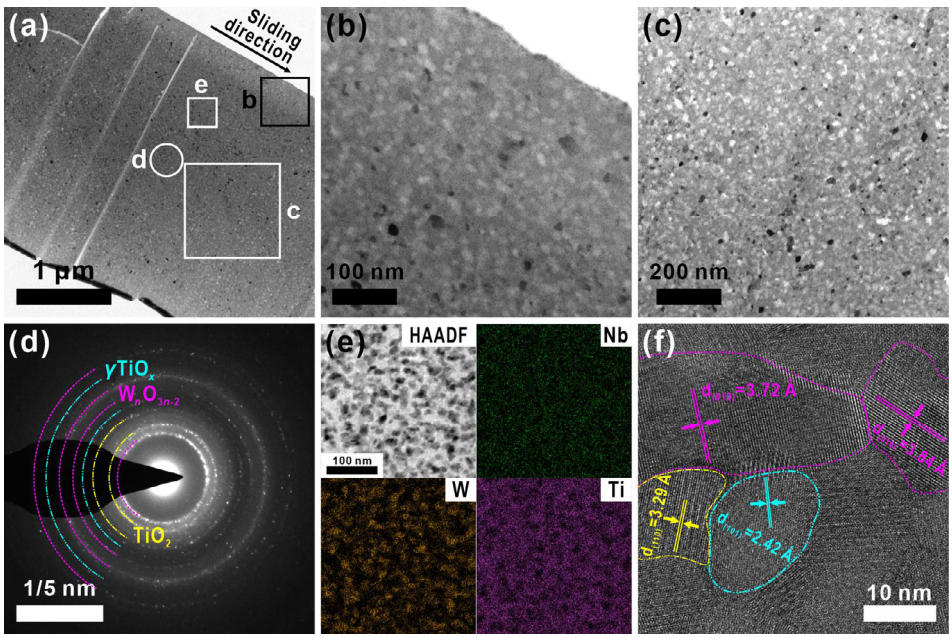

Fig. 5 (a) Cross-sectional bright-field TEM image of the TiNbWN thin film after sliding against 316ss stainless steel for a test distance of 18 m at 750 °C. Note that the penetrating cracks are generated during thinning of the sample using FIB. (b, c) Enlarged bright-field TEM images of the region marked as "b" and "c" in (a), respectively, showing that the thin film consists of dark and white nanoparticles. (d) SAED pattern taken from the region marked as "d" in (a). (e) HAADF image and corresponding EDS mappings of the region marked as "e" in (a). (f) Representative HRTEM image showing the formation of nano W_nO_{3n-2}, TiO_2, and γTiO_x crystals in the TiNbWN thin film.

compositions of the W-rich and Ti-rich regions (areas) were acquired through the EDS point measurements and are provided in Table 1. The nano-grain boundaries of W_nO_{3n-2}, TiO_2, and γTiO_x crystallites are demarcated in the HRTEM images using purple dash lines, yellow dash-dot lines, and cyan-blue dash-dot-dot lines, respectively. Measured interplanar spacing of W_nO_{3n-2} (010), TiO_2 (110), and γTiO_x (101) planes are 3.7, 3.3, and 2.4 Å, respectively.

The formation of nanocrystalline oxides in the TiNbWN thin film during high-temperature sliding (750 °C) resulted in a significant reduction of the grain size and could enhance H in accordance with the Hall–Petch relationship [53]:

$$H = H_0 + k \times d^{-\frac{1}{2}} \tag{2}$$

where H_0 is the hardness value for large grain sizes, d is the average grain size of the material, and k is the strengthening coefficient (a constant specific to each material). According to Eq. (2), the increment of hardness (ΔH) induced by the grain size variation (Δd) can be calculated using Eq. (3):

$$\Delta H = k \times \left(d_1^{-\frac{1}{2}} - d_2^{-\frac{1}{2}} \right) \tag{3}$$

in which d_1 and d_2 are the average grain sizes of the material before and after grain refinement, respectively. Here, an experimentally-determined k value of ~10.2 GPa·(nm)$^{1/2}$ for titanium oxide was used for general estimates [54, 55]. The average grain sizes of the as-deposited thin film and the one after high-temperature sliding were determined from Figs. 1 and 5 ($d_m \approx 140$ nm and $d_n \approx 18.1$ nm). Hence, the calculated ΔH as per the Hall–Petch relationship was ~1.5 GPa. The grain refinement may conceivably cause the slight increment of the hardness of the film at 750 °C.

Table 1 Chemical compositions of the W-rich and Ti-rich regions obtained by the EDS point measurements.

	N (at%)	O (at%)	Ti (at%)	Nb (at%)	W (at%)
W-rich region	0.0	62.8	2.1	13.8	21.3
Ti-rich region	9.2	58.6	23.9	3.5	4.8

3.4 Formation temperature of nanocrystalline oxides

Figure 6(a) shows the representative Raman spectra taken from the wear tracks of the TiNbWN thin film after the sliding tests at different temperatures. Characteristic peaks at 260, 334, 734, and 805 cm^{-1} indicate the presence of the W_nO_{3n-2} phase on the wear track of the thin film generated at 750 °C [56–58], which cannot be detected on the worn surfaces at lower temperatures. One should note that the generated tungsten oxides at 750 °C were possibly the W_nO_{3n-2} phase (one of the Magnéli phase) rather than the WO_3 phase [34, 36, 59–61]. According to the literature, the W_nO_{3n-2} phase with an oxygen deficiency possesses a crystal structure with ordered patterns of edge-sharing octahedra within the ReO_3-like network, leading to the emerging of easy crystallographic shear planes [62]. It was found that Magnéli phases could be formed on the surfaces of Ti-, V-, Mo-, W-, or Nb-containing materials upon sliding or oxidation at elevated temperatures [34, 36, 61, 63]. The present results of Raman spectra and TEM observations suggest the formation of W_nO_{3n-2} in the film. Besides, the formation

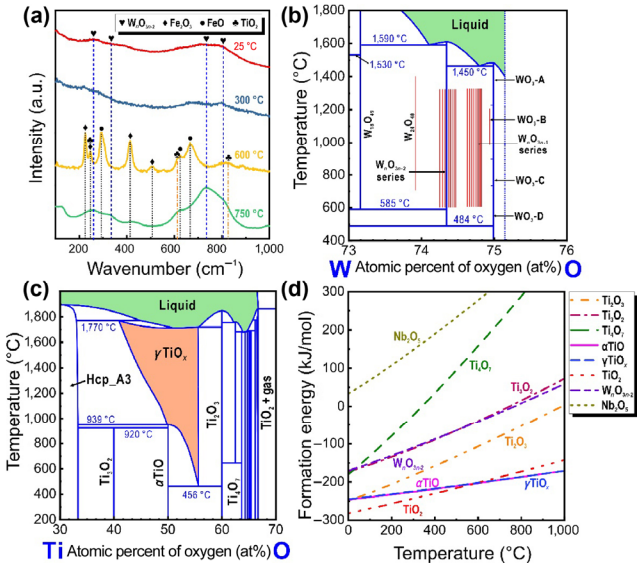

Fig. 6 (a) Representative Raman spectra taken from the wear tracks of the TiNbWN thin film sliding against 316ss stainless steel at 25, 300, 600, and 750 °C. (b) Phase diagrams of W–O system with the oxygen concentration from 73 to 76 at% and (c) Ti–O system in the oxygen concentration range between 30 and 70 at%. (d) Calculated formation energies (G_{form}) of the selected oxides in the Ti–Nb–W–N–O system, indicating that the TiO_2, γTiO_x, and W_nO_{3n-2} are thermodynamically preferable to form.

of TiO_2 after sliding at 600 and 750 °C was confirmed by the characteristic peaks at 246, 612, and 825 cm^{-1} in the Raman spectra [23, 64]. The formation temperature of the W_nO_{3n-2} oxides was further rationalized using the W–O phase diagram [59] shown in Fig. 6(b). A threshold temperature at ~585 °C for the formation of the W_nO_{3n-1} and W_nO_{3n-2} series was noted, which was also supported by the relevant literature [37, 63, 65]. For example, Polcar et al. [65] demonstrated the formation temperature of tungsten oxides on the WN film at ~500 °C. Liu et al. [37] argued that the critical oxidizing temperature of WC is between 500 and 550 °C, and the tungsten oxides became detectable at 550 °C. Using differential scanning calorimetric and simultaneous thermo-gravimetric analysis, Gassner et al. [63] found the oxidation threshold of the WN thin film to be ~550 °C. Their experimental results also indicated that a large quantity of oxides could only form when the temperature exceeded ~650 °C [63]. Thus, it can be inferred that the amount of W_nO_{3n-2} phase generated at 600 °C was insufficient to maintain a stable oxide layer to reduce wear, whereas bulk oxidation of the TiNbWN film at 750 °C facilitated a wear reduction as a result of both hardness enhancement and a solid-lubrication effect.

Figure 6(c) shows the phase diagram of the Ti–O system calculated using CALPHAD approach [66–68] based on the well-accepted thermodynamic dataset from the literature [52]. The γTiO_x phase (marked in orange) is shown in the phase diagram, which exhibits a wide solubility range (from ~ 41.2 to 56.7 at% O) and a threshold formation temperature at ~456 °C. Since it stretches over wide composition and temperature ranges in the phase diagram, γTiO_x is supposed to possess a high thermal stability, especially at high temperatures. Additionally, there are a number of stoichiometric compounds existing in the Ti–O phase diagram, such as Ti_3O_2, αTiO, and Ti_4O_7. The G_{form} of selected oxides were further obtained to compare their thermodynamic stabilities. G_{form} of a compound A_nB_m can be calculated using Eq. (4):

$$G_{form} = G(A_nB_m) - \left(\frac{n}{n+m}G(A) + \frac{m}{n+m}G(B)\right) \quad (4)$$

in which G(A) and G(B) present the Gibbs energies of Components A and B at their reference states, respectively. G(A) and G(B) can be obtained using the CALPHAD approach. Figure 6(d) shows the calculated G_{form} of the selected oxides. Among the selected oxides, TiO_2 contains the lowest G_{form} at temperatures below ~600 °C, while γTiO_x becomes more thermodynamically preferable at higher temperatures. As for tungsten and niobium oxides, it appears that W_nO_{3n-2} contains much lower G_{form} than Nb_2O_5. The calculated results demonstrated that the TiO_2, γTiO_x, and W_nO_{3n-2} binary oxides are thermodynamically preferable to form in the Ti–Nb–W–N–O system, which is highly in agreement with the current experimental observations.

To clarify the effect of TiO_2, γTiO_x, and W_nO_{3n-2} formation on the wear performance of TiNbWN film, we investigated the adhesion behavior of the pristine and oxidized TiNbWN films against the sliding counterfaces by employing *ab initio* calculations. Due to the complexity of wear mechanisms, rough approximations at the DFT level are made to mimic the real physical interactions and provide the general trends. Since the 316ss counterface could easily be oxidized during sliding, FeO instead of pure iron or steel was considered as an adsorbate in all the adsorption calculations. Additionally, the calculations narrowed down to the adsorption on the (001) surface due to its lower surface energy compared with other crystallographic planes in an fcc structure [69], and it is one of the facets obtained in this work (Fig. 1). The calculated adsorption energies of FeO molecule on the WO_3(001), TiO_2(001), and TiNbWN(001) surfaces are shown in Fig. 7(a), in which typical slab models with the O atom approaching the surface metal atoms are presented. Although the lateral size of the considered configurations is not the same, only minor deviations in the adsorption energy can be expected based on the previous work [70]. The present results show that the FeO molecules with O end toward the surface of WO_3(001), TiO_2(001), and TiNbWN(001) exhibit lower adsorption energies compared with the FeO molecule with Fe end (notated here as *OFe*), demonstrating that there are stronger adhesions between O atoms and the metal atoms on crystal surfaces. The TiNbWN(001) surface exhibits the lowest adsorption energy (the strongest interaction) compared with the TiO_2(001) and WO_3(001) surfaces, when

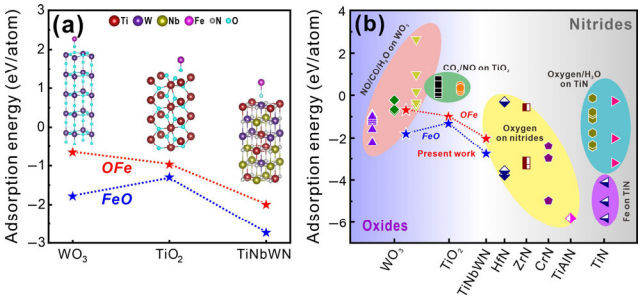

Fig. 7 (a) Calculated adsorption energies of iron oxide molecule on the WO_3(001), TiO_2(001), and TiNbWN(001) surfaces with the slab models inserted. Notations *FeO* and *OFe* pertain to the orientations of the FeO molecule atop the surfaces. The insets show the *FeO* case. The VASP code was employed. (b) Summary of the reported adsorption energies of species and molecules on various surfaces [71–83] compared with the currently calculated adsorption energies.

considering both *FeO* and *OFe* orientations of iron oxides. This indicates that when the oxides were formed on the surface of TiNbWN films, the interfacial adhesion could be distinctly mitigated, leading to the improved performance of friction and wear.

We further compared our calculation results with the literature pertaining to the adsorption of other substances on various surfaces, as shown in Fig. 7(b). The adsorption energy on the WO_3 surface varied in a range of −1.25–0.97 eV/atom, depending on the types of adsorbates (NO, CO, or H_2O) [71–75], while those of NO and CO_2 on the TiO_2 surface were in a narrow range of 0.03–0.74 eV/atom [76–78]. As for the nitride surfaces, the adsorption sites obviously impact the adsorption energies [79–81]. The interaction between oxygen/H_2O molecules and the metal atoms in the nitrides was considerably stronger, resulting in a lower adsorption energy [80, 81]. Furthermore, the Fe atom adsorbed strongly on TiN(001) surface, exhibiting the adsorption energies in the range of −5.81–(−4.12) eV/atom at different adsorption sites. The currently calculated adsorption energies of iron oxides with the O end (*FeO*) varied between −2.73 and −1.30 eV/atom, which was within the adsorption energy range of NO/CO/H_2O on WO_3 and oxygen on nitrides, and slightly lower than the adsorption energy of CO_2/NO on TiO_2. FeO with the Fe end (*OFe*), however, exhibited slightly weaker interactions with the WO_3(001), TiO_2(001), and TiNbWN(001) surfaces and contained higher adsorption energies (−2.00–(−0.66) eV/atom). Clearly, the TiNbWN outperforms the benchmark coating TiN since the interaction with oxidized steel surfaces (wear counterpart) is considerably weaker. Based on the calculation results, the WO_3 and TiO_2 oxides are expected to achieve an ameliorated adhesion with the iron oxide in comparison with the TiNbWN film, which is consistent with the experimental data. Hence, by combining the CALPHAD and DFT results, the wear mechanism transition of the TiNbWN film between 600–750 °C can be delineated as follows: (i) When the sliding temperature reaches ~600 and 750 °C, a large quantity of tungsten and titanium oxides readily form (Fig. 6); (ii) mechanical properties of the film could be slightly enhanced, following the Hall–Petch relationship (Section 3.3), thus increasing the wear resistance; (iii) the tungsten and titanium oxides can obviously alleviate the interface adhesion between the film and the sliding counterparts, as suggested by DFT calculations (Fig. 7). Therefore, the nano-oxides generated at high temperatures could act as solid lubricants to reduce wear losses.

4 Conclusions

We have designed and synthesized a new MEN film, TiNbWN, with a near-equiatomic composition and an fcc solution using a reactive magnetron sputtering. The wear performances of the thin film at a temperature range of 25–750 °C were examined. In the temperature range of 25–600 °C, the wear resistance of the film was dependent on the surface hardness, which decreased monotonously as the temperature rose. At a higher temperature (750 °C), the nanocrystalline oxides (W_nO_{3n-2}, TiO_2, and γTiO_x) were formed during sliding, enhancing the hardness of the film and providing solid lubrication, both of which contributed to a reduced wear loss. This is corroborated theoretically on both continuum and atomic level. Thus, the work presented herein delineated the role of the *in situ* formed nanocrystalline oxides in the wear mechanism transition of TiNbWN thin films, which could in general shed light on the high-temperature wear behavior of refractory HEN/MEN films.

Acknowledgements

Financial support from the National Natural Science Foundation of China (52142501 and 52101026), the National Key R&D Program of China (2018YFA0703400), Natural Science Foundation of Zhejiang Province (LQ20E010004), China Postdoctoral Science Foundation (2021M693250), Ningbo 3315 Innovation Team (2019A-18-C), CAS PIFI program (2022VEA0005), and CAS Pioneer Hundred Talents Program are greatly acknowledged.

Declaration of competing interest

The authors have no competing interests to declare that are relevant to the content of this article.

Open Access This article is licensed under a Creative Commons Attribution 4.0 International License, which permits use, sharing, adaptation, distribution and reproduction in any medium or format, as long as you give appropriate credit to the original author(s) and the source, provide a link to the Creative Commons licence, and indicate if changes were made.

The images or other third party material in this article are included in the article's Creative Commons licence, unless indicated otherwise in a credit line to the material. If material is not included in the article's Creative Commons licence and your intended use is not permitted by statutory regulation or exceeds the permitted use, you will need to obtain permission directly from the copyright holder.

To view a copy of this licence, visit http://creativecommons.org/licenses/by/4.0/.

References

[1] Yeh J W, Chen S K, Lin S J, Gan J Y, Chin T S, Shun T T, Tsau C H, Chang S Y. Nanostructured high-entropy alloys with multiple principal elements: Novel alloy design concepts and outcomes. *Adv Eng Mater* **6**(5): 299–303 (2004)

[2] George E P, Raabe D, Ritchie R O. High-entropy alloys. *Nat Rev Mater* **4**(8): 515–534 (2019)

[3] Cantor B, Chang I T H, Knight P, Vincent A J B. Microstructural development in equiatomic multicomponent alloys. *Mater Sci Eng A* **375–377**: 213–218 (2004)

[4] Zhang Y. Materials design of high-entropy materials. In: *High-Entropy Materials: A Brief Introduction*. Singapore: Springer Singapore, 2019: 35–63.

[5] Oses C, Toher C, Curtarolo S. High-entropy ceramics. *Nat Rev Mater* **5**(4): 295–309 (2020)

[6] Moon J, Park J M, Bae J W, Do H S, Lee B J, Kim H S. A new strategy for designing immiscible medium-entropy alloys with excellent tensile properties. *Acta Mater* **193**: 71–82 (2020)

[7] Lewin E. Multi-component and high-entropy nitride coatings—A promising field in need of a novel approach. *J Appl Phys* **127**(16): 160901 (2020)

[8] Shu R, Paschalidou E M, Rao S G, Lu J, Greczynski G, Lewin E, Nyholm L, le Febvrier A, Eklund P. Microstructure and mechanical, electrical, and electrochemical properties of sputter-deposited multicomponent (TiNbZrTa)N_x coatings. *Surf Coat Technol* **389**: 125651 (2020)

[9] Shu R, Paschalidou E M, Rao S G, Bakhit B, Boyd R, Moro M V, Primetzhofer D, Greczynski G, Nyholm L, le Febvrier A, et al. Effect of nitrogen content on microstructure and corrosion resistance of sputter-deposited multicomponent (TiNbZrTa)N_x films. *Surf Coat Technol* **404**: 126485 (2020)

[10] Baran Ö. Manetron Sıçratma Yöntemiyle Kaplanmış TiNbN ve TiVN Filmlerin Mekanik ve Tribolojik Özelliklerinin İncelenmesi. *Gümüşhane Üniversitesi Fen Bilimleri Enstitüsü Dergisi* **7**(2): 181–191 (2017) (in Turkish)

[11] Serro A P, Completo C, Colaço R, dos Santos F, da Silva C L, Cabral J M S, Araújo H, Pires E, Saramago B. A comparative study of titanium nitrides, TiN, TiNbN and TiCN, as coatings for biomedical applications. *Surf Coat Technol* **203**(24): 3701–3707 (2009)

[12] Zhou S, Liu W G, Liu H, Cai C L. Structural and electrical properties of Ti–W–N thin films deposited by reactive RF sputtering. *Phys Procedia* **18**: 66–72 (2011)

[13] Shaginyan L R, Mišina M, Zemek J, Musil J, Regent F, Britun V F. Composition, structure, microhardness and residual stress of W–Ti–N films deposited by reactive magnetron sputtering. *Thin Solid Films* **408**(1–2): 136–147 (2002)

[14] Kuchuk A V, Kladko V P, Lytvyn O S, Piotrowska A, Minikayev R A, Ratajczak R. Relationship between condition of deposition and properties of W–Ti–N thin films prepared by reactive magnetron sputtering. *Adv Eng Mater* **8**(3): 209–212 (2006)

[15] Cavaleiro A, Trindade B, Vieira M T. Influence of Ti addition on the properties of W–Ti–C/N sputtered films. *Surf Coat Technol* **174–175**: 68–75 (2003)

[16] Jalali R, Parhizkar M, Bidadi H, Naghshara H, Eshraghi M J. Characterization of nano-crystalline Ti–W–N thin films for

diffusion barrier application: A structural, microstructural, morphological and mechanical study. *Appl Phys A* **124**(12): 810 (2018)

[17] Jalali R, Parhizkar M, Bidadi H, Naghshara H. Correlation between optical, structural and microstructural properties of Ti–W–N thin films. *Ceram Int* **46**(5): 6454–6461 (2020)

[18] Kitamika Y, Shingu H, Tanigawa S, Hasegawa H. Mechanical properties and oxidation resistance of $Ti_{1-x}W_xN$ coatings. *J Surf Finish Soc Jpn* **69**(11): 517–520 (2018)

[19] Lou M, Chen X, Xu K, Deng Z X, Chen L L, Lv J, Chang K K, Wang L P. Temperature-induced wear transition in ceramic–metal composites. *Acta Mater* **205**: 116545 (2021)

[20] Meng Y G, Xu J, Jin Z M, Prakash B, Hu Y Z. A review of recent advances in tribology. *Friction* **8**(2): 221–300 (2020)

[21] Chen X, Han Z. A low-to-high friction transition in gradient nano-grained Cu and Cu–Ag alloys. *Friction* **9**(6): 1558–1567 (2021)

[22] Lou M, White D R, Banerji A, Alpas A T. Dry and lubricated friction behaviour of thermal spray low carbon steel coatings: Effect of oxidational wear. *Wear* **432–433**: 102921 (2019)

[23] Lou M, Alpas A T. High temperature wear mechanisms in thermally oxidized titanium alloys for engine valve applications. *Wear* **426–427**: 443–453 (2019)

[24] Yang R, Ma W, Duan C J, Li S, Wang T M, Wang Q H. Self-lubrication of tribologically-induced oxidation during dry reciprocating sliding of aged Ti–Ni51.5 at% alloy. *Friction* **9**(5): 1038–1049 (2021)

[25] Fink M. Wear oxidation—A new component of wear. *T Am Soc Steel Treating* **18**:1026–1034 (1930)

[26] Stott F H. The role of oxidation in the wear of alloys. *Tribol Int* **31**(1–3): 61–71 (1998)

[27] Cui X H, Wang S Q, Wang F, Chen K M. Research on oxidation wear mechanism of the cast steels. *Wear* **265**(3–4): 468–476 (2008)

[28] Childs T H C. The sliding wear mechanisms of metals, mainly steels. *Tribol Int* **13**(6): 285–293 (1980)

[29] Dohda K, Boher C, Rezai-Aria F, Mahayotsanun N. Tribology in metal forming at elevated temperatures. *Friction* **3**(1): 1–27 (2015)

[30] Dong X, Jahanmir S. Wear transition diagram for silicon nitride. *Wear* **165**(2): 169–180 (1993)

[31] Zhou Z, Rainforth W M, Luo Q, Hovsepian P E, Ojeda J J, Romero-Gonzalez M E. Wear and friction of TiAlN/VN coatings against Al_2O_3 in air at room and elevated temperatures. *Acta Mater* **58**(8): 2912–2925 (2010)

[32] Javdošňák D, Musil J, Soukup Z, Haviar S, Čerstvý R, Houska J. Tribological properties and oxidation resistance of tungsten and tungsten nitride films at temperatures up to 500 °C. *Tribol Int* **132**: 211–220 (2019)

[33] Moghaddam P V, Prakash B, Vuorinen E, Fallqvist M, Andersson J M, Hardell J. High temperature tribology of TiAlN PVD coating sliding against 316L stainless steel and carbide-free bainitic steel. *Tribol Int* **159**: 106847 (2021)

[34] Magnéli A. Structures of the ReO_3-type with recurrent dislocations of atoms: "Homologous series" of molybdenum and tungsten oxides. *Acta Crystallogr* **6**: 495–500 (1953)

[35] Woydt M, Skopp A, Dörfel I, Witke K. Wear engineering oxides/anti-wear oxides. *Wear* **218**(1): 84–95 (1998)

[36] Migas D B, Shaposhnikov V L, Borisenko V E. Tungsten oxides. II. The metallic nature of Magnéli phases. *J Appl Phys* **108**(9): 093714 (2010)

[37] Liu Y L, Wang Z X, Sun Q C, Yin B, Cheng J, Zhu S Y, Yang J, Qiao Z H, Liu W M. Tribological behavior and wear mechanism of pure WC at wide range temperature from 25 to 800 °C in vacuum and air environment. *Int J Refract Met Hard Mater* **71**: 160–166 (2018)

[38] Lugscheider E, Knotek O, Bobzin K, Bärwulf S. Tribological properties, phase generation and high temperature phase stability of tungsten- and vanadium-oxides deposited by reactive MSIP–PVD process for innovative lubrication applications. *Surf Coat Technol* **133–134**: 362–368 (2000)

[39] Suszko T, Gulbiński W, Jagielski J. The role of surface oxidation in friction processes on molybdenum nitride thin films. *Surf Coat Technol* **194**(2–3): 319–324 (2005)

[40] Oliver W C, Pharr G M. An improved technique for determining hardness and elastic modulus using load and displacement sensing indentation experiments. *J Mater Res* **7**(6): 1564–1583 (1992)

[41] Hohenberg P, Kohn W. Inhomogeneous electron gas. *Phys Rev* **136**(3B): B864–B871 (1964)

[42] Kresse G, Hafner J. *Ab initio* molecular-dynamics simulation of the liquid–metal–amorphous–semiconductor transition in germanium. *Phys Rev B* **49**(20): 14251–14269 (1994)

[43] Kresse G, Joubert D. From ultrasoft pseudopotentials to the projector augmented-wave method. *Phys Rev B* **59**(3): 1758–1775 (1999)

[44] Blöchl P E. Projector augmented-wave method. *Phys Rev B* **50**(24): 17953–17979 (1994)

[45] Predel F. *Phase Equilibria, Crystallographic and Thermodynamic Data of Binary Alloys*. Heidelberg (Germany): Springer Berlin Heidelberg, 2016.

[46] Huang W M. Thermodynamic assessment of the Nb–N system. *Metall Mater Trans A* **27**(11): 3591–3600 (1996)

[47] Miao K F, Wang J, Zhao Q, Wang K W, Wen M, Zhang K. Water-based lubrication of niobium nitride. *Friction* **10**(6): 842–853 (2022)

[48] Lin J L, Moore J J, Mishra B, Pinkas M, Sproul W D. The structure and mechanical and tribological properties of

TiBCN nanocomposite coatings. *Acta Mater* **58**(5): 1554–1564 (2010)

[49] Leyland A, Matthews A. On the significance of the *H*/*E* ratio in wear control: A nanocomposite coating approach to optimised tribological behaviour. *Wear* **246**(1–2): 1–11 (2000)

[50] Archard J F, Hirst W. The wear of metals under unlubricated conditions. *Proc Roy Soc A Math Phy Sci* **236**(1206): 397–410 (1956)

[51] Hutchings I, Shipway P. *Tribology: Friction and Wear of Engineering Materials*, 2nd edn. Oxford (UK): Butterworth–Heinemann, 2017.

[52] Hampl M, Schmid-Fetzer R. Thermodynamic description of the Ti–O system. *Int J Mater Res* **106**(5): 439–453 (2015)

[53] Erb U, Palumbo G, McCrea J L. The processing of bulk nanocrystaline metals and alloys by electrodeposition. In: *Nanostructured Metals and Alloys: Processing, microstructure, mechanical properties and applications*, Whang S H, Ed. Cambridge (UK): Woodhead Publishing, 2011: 118–151.

[54] Li Y, Song K F. Study on manufacture process, micro-hardness and Hall–Petch relation of pure rutile phase TiO_2 MAO coating. *Appl Mech Mater* **738–739**: 175–179 (2015)

[55] Bahador A, Umeda J, Hamzah E, Yusof F, Li X C, Kondoh K. Synergistic strengthening mechanisms of copper matrix composites with TiO_2 nanoparticles. *Mater Sci Eng A* **772**: 138797 (2020)

[56] Chen J, Lu D Y, Zhang W H, Xie F Y, Zhou J, Gong L, Liu X, Deng S Z, Xu N S. Synthesis and Raman spectroscopic study of $W_{20}O_{58}$ nanowires. *J Phys D Appl Phys* **41**(11): 115305 (2008)

[57] Sun L, Li Z, Su R, Wang Y L, Li Z L, Du B S, Sun Y, Guan P F, Besenbacher F, Yu M. Phase-transition induced conversion into a photothermal material: Quasi-metallic $WO_{2.9}$ nanorods for solar water evaporation and anticancer photothermal therapy. *Angew Chem Int Ed* **57**(33): 10666–10671 (2018)

[58] Pirker L, Višić B, Škapin S D, Dražić G, Kovač J, Remškar M. Multi-stoichiometric quasi-two-dimensional W_nO_{3n-1} tungsten oxides. *Nanoscale* **12**(28): 15102–15114 (2020)

[59] Wriedt H A. The O–W (oxygen–tungsten) system. *Bull Alloy Phase Diagr* **10**(4): 368–384 (1989)

[60] Kutschej K, Mayrhofer P H, Kathrein M, Polcik P, Mitterer C. A new low-friction concept for $Ti_{1-x}Al_xN$ based coatings in high-temperature applications. *Surf Coat Technol* **188–189**: 358–363 (2004)

[61] Reeswinkel T, Music D, Schneider J M. Coulomb-potential-dependent decohesion of magnéli phases. *J Phys Condens Matter* **22**(29): 292203 (2010)

[62] Lugscheider E, Bärwulf S, Barimani C. Properties of tungsten and vanadium oxides deposited by MSIP–PVD process for self-lubricating applications. *Surf Coat Technol* **120–121**: 458–464 (1999)

[63] Gassner G, Mayrhofer P H, Kutschej K, Mitterer C, Kathrein M. Magnéli phase formation of PVD Mo–N and W–N coatings. *Surf Coat Technol* **201**(6): 3335–3341 (2006)

[64] Zhang J, Li M J, Feng Z C, Chen J, Li C. UV Raman spectroscopic study on TiO_2. I. Phase transformation at the surface and in the bulk. *J Phys Chem B* **110**(2): 927–935 (2006)

[65] Polcar T, Parreira N M G, Cavaleiro A. Structural and tribological characterization of tungsten nitride coatings at elevated temperature. *Wear* **265**(3–4): 319–326 (2008)

[66] Xu K, Chang K K, Yu M, Zhou D P, Du Y, Wang L P. Design of novel NiSiAlY alloys in marine salt-spray environment: Part II. Al–Ni–Si–Y thermodynamic dataset. *J Mater Sci Technol* **89**: 186–198 (2021)

[67] Xu K, Chang K K, Zhou X B, Chen L L, Liu J W, Deng Z X, Huang F, Huang Q. Thermodynamic descriptions of the light rare-earth elements in silicon carbide ceramics. *J Am Ceram Soc* **103**(6): 3812–3825 (2020)

[68] Liu S D, Chang K K, Music D, Chen X, Mráz S, Bogdanovski D, Hans M, Primetzhofer D, Schneider J M. Stress-dependent prediction of metastable phase formation for magnetron-sputtered $V_{1-x}Al_xN$ and $Ti_{1-x}Al_xN$ thin films. *Acta Mater* **196**: 313–324 (2020)

[69] Wang C, Dai Y B, Gao H Y, Ruan X M, Wang J, Sun B D. Surface properties of titanium nitride: A first-principles study. *Solid State Commun* **150**(29–30): 1370–1374 (2010)

[70] Riedl H, Zálešák J, Arndt M, Polcik P, Holec D, Mayrhofer P H. *Ab initio* studies on the adsorption and implantation of Al and Fe to nitride materials. *J Appl Phys* **118**(12): 125306 (2015)

[71] Zhao L H, Tian F H, Wang X B, Zhao W W, Fu A P, Shen Y Y, Chen S G, Yu S Q. Mechanism of CO adsorption on hexagonal WO_3 (001) surface for gas sensing: A DFT study. *Comput Mater Sci* **79**: 691–697 (2013)

[72] Saadi L, Lambert-Mauriat C, Oison V, Ouali H, Hayn R. Mechanism of NO_x sensing on WO_3 surface: First principle calculations. *Appl Surf Sci* **293**: 76–79 (2014)

[73] Oison V, Saadi L, Lambert-Mauriat C, Hayn R. Mechanism of CO and O_3 sensing on WO_3 surfaces: First principle study. *Sens Actuat B Chem* **160**(1): 505–510 (2011)

[74] Hurtado-Aular O, Vidal A B, Sierraalta A, Añez R. Periodic DFT study of water adsorption on m-WO_3(001), m-WO_3(100), h-WO_3(001) and h-WO_3(100). Role of hydroxyl groups on the stability of polar hexagonal surfaces. *Surf Sci* **694**: 121558 (2020)

[75] Albanese E, di Valentin C, Pacchioni G. H_2O adsorption on WO_3 and WO_{3-x}(001) surfaces. *ACS Appl Mater Interfaces* **9**(27): 23212–23221 (2017)

[76] Sorescu D C, Rusu C N, Yates J T. Adsorption of NO on the TiO_2(110) surface: An experimental and theoretical study. *J Phys Chem B* **104**(18): 4408–4417 (2000)

[77] Sorescu D C, Yates J T. Adsorption of CO on the TiO_2(110) surface: A theoretical study. *J Phys Chem B* **102**(23): 4556–4565 (1998)

[78] Klyukin K, Alexandrov V. CO_2 adsorption and reactivity on rutile TiO_2(110) in water: An *ab initio* molecular dynamics study. *J Phys Chem C* **121**(19): 10476–10483 (2017)

[79] Wang C, Dai Y B, Gao H Y, Ruan X M, Wang J, Sun B D. *Ab initio* molecular dynamics study of Fe adsorption on TiN (001) surface. *Mater Trans* **51**(11): 2005–2008 (2010)

[80] Kang Q X, Wang G F, Liu Q, Sui X C, Liu Y K, Chen Y Q, Luo S Y, Li Z L. Investigation for oxidation mechanism of CrN: A combination of DFT and *ab initio* molecular dynamics study. *J Alloys Compd* **885**: 160940 (2021)

[81] Guo F Y, Wang J C, Du Y, Wang J, Shang S L, Li S L, Chen L. First-principles study of adsorption and diffusion of oxygen on surfaces of TiN, ZrN and HfN. *Appl Surf Sci* **452**: 457–462 (2018)

[82] Music D, Schneider J M. *Ab initio* study of $Ti_{0.5}Al_{0.5}N$(001)—residual and environmental gas interactions. *New J Phys* **15**(7): 073004 (2013)

[83] Sanyal S, Waghmare U V, Ruud J A. Adsorption of water on TiN(100), (110) and (111) surfaces: A first-principles study. *Appl Surf Sci* **257**(15): 6462–6467 (2011)

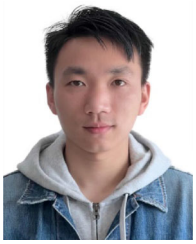

Leilei CHEN. He received his bachelor degree in 2016 from Wuhan University of Science and Technology, Wuhan, China. In 2019, he obtained his M.E. degree in mechanical engineering from Dalian University of Technology, Dalian, China. His is currently a Ph.D. student in the Key Laboratory for Precision and Non-Traditional Machining Technology of Ministry of Education at Dalian University of Technology. His research interests include friction performances and wear mechanisms of the physical vapour deposition (PVD) nitride films.

Zhenyu ZHANG. He received his B.E. degree in mechanical engineering in 2000 from Hebei Institute of Science and Technology, Tangshan, China. In 2003, he received M.E. degree in mechanical engineering from Hebei University of Technology, Tianjin, China. After that, he obtained his Ph.D. degree in 2005 in solid mechanics from Tianjin University, Tianjin, China. His current position is a professor in mechanical engineering at Dalian University of Technology, Dalian, China. His research interests focus on precision and ultra-precision machining technologies, and high performance manufacturing.

Keke CHANG. He received his bachelor and master degrees from Central South University, Changsha, China, in 2008 and 2010, respectively, and Ph.D. degree from RWTH Aachen University, Germany, in 2013. He is now a professor at Ningbo Institute of Materials Technology and Engineering, Chinese Academy of Sciences, Ningbo, China. His research interest is theoretical design of coatings, surfaces, and interfaces for serving in harsh environments.